

Dualband Split Dielectric Resonator Antenna

Tze-Hsuan Chang, *Student Member, IEEE*, and Jean-Fu Kiang, *Member, IEEE*

Abstract—A dualband dielectric resonator antenna (DRA) is designed by splitting a rectilinear dielectric resonator (DR) and carving notches off the DR. It is observed that notches engraved at different positions affect different modes. Removal of dielectric material from where the electric field is strong incurs a significant increase in resonant frequency. The abrupt change of normal electric field across the discontinuities reduces the Q -factor and increases the impedance bandwidth. Both the TE_{111}^y and TE_{113}^y modes incur broadside radiation patterns on the xy -plane. The proposed DRA can cover both the worldwide interoperability for microwave access (WiMAX, 3.4–3.7-GHz) and the wireless local area network (WLAN, 5.15–5.35-GHz) bands.

Index Terms—Dielectric resonator (DR).

I. INTRODUCTION

DIELECTRIC resonators made of low-loss and high-permittivity material have been used to implement antennas [1]. They have higher radiation efficiency than printed antennas at higher frequency due to the absence of ohmic loss and surface wave, in addition to compact size, light weight, and low cost.

Many efforts have been devoted to developing multiband or wideband dielectric resonator antennas (DRAs) [2]–[15]. For example, make the feeding aperture radiate like a slot antenna to incur another band [2]–[4] and induce parasitic effects with attached metal strips [5]–[7].

In [8], specific higher order modes with the electric field distribution on the top surface of the dielectric resonator (DR) similar to that of the fundamental mode are intentionally excited. In [9] and [10], higher order modes of truncated conical or tetrahedral DR are excited to obtain wide impedance bandwidth.

DRs of different sizes have been placed vertically to form a stacked DRA, or at close proximity, to form a multielement DRA to attain wideband or dualband features [12]–[15].

In this paper, a dualband DR antenna is proposed by splitting a rectilinear DR evenly. The electric field over the gap in between is significantly enhanced, hence reducing the Q -factor. Two notches are also engraved in each piece to tune the resonant frequencies and increase the impedance bandwidth as well. The effect of the gap and notches on the resonant frequencies are carefully studied and the resonant bands associated with the TE_{111}^y and TE_{113}^y modes can be adjusted to cover the worldwide interoperability for microwave access (WiMAX, 3.4–3.7-GHz) and the wireless local area network (WLAN, 5.15–5.35-GHz) bands.

Manuscript received January 20, 2007; revised May 1, 2007. This work was supported by the National Science Council, Taiwan, under Contract NSC 93-2213-E-002-034.

The authors are with the Department of Electrical Engineering and the Graduate Institute of Communication Engineering, National Taiwan University, Taipei 106, Taiwan (e-mail: jfkiang@cc.ee.ntu.edu.tw).

Digital Object Identifier 10.1109/TAP.2007.908830

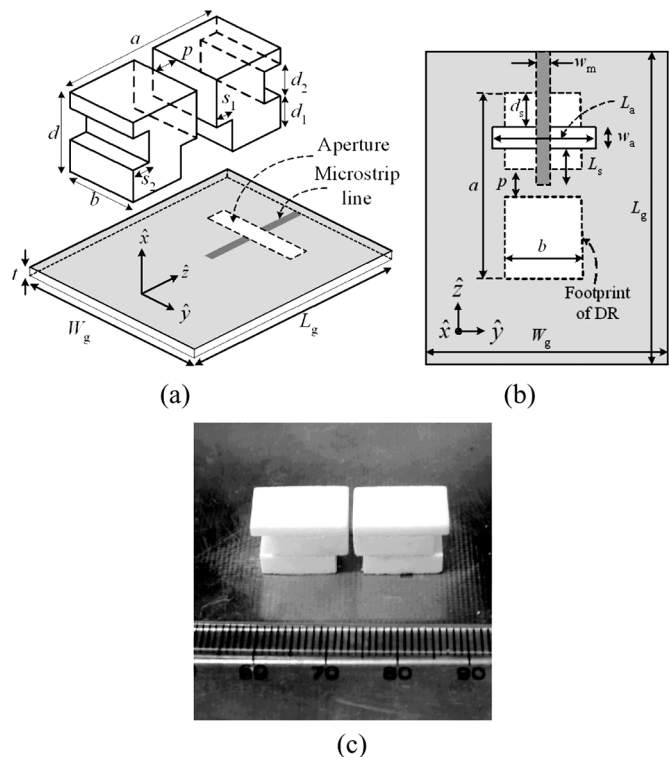


Fig. 1. Configuration of split DRA. (a) Panoramic view. (b) Top view. (c) Photograph.

II. ANTENNA CONFIGURATION

Fig. 1 shows the configuration of the DRA, which is composed of two identical rectangular DRs of dimension $a \times b \times d$, separated by a gap p . Each DR is engraved with two notches at its bottom and side edge, with dimensions $s_1 \times b \times d_1$ and $s_2 \times b \times d_2$, respectively. The DRs are placed on a ground plane of size $W_g \times L_g$ on an FR4 substrate of thickness t and permittivity 4.4. A microstrip line is used to feed the DRs through an aperture of size $L_a \times W_a$. The microstrip line is extended over the aperture by L_s . The offset between the aperture and the DR is d_s .

The resonant frequency is mainly determined by the DR dimensions a, b, d and permittivity $\epsilon_0 \epsilon_r$. The carved notches change the electric field distribution in the original DRs, hence the resonant frequencies. Since the gap is perpendicular to the electric field of the TE_{111}^y mode of the otherwise intact DR, the electric field is enhanced within the gap. Thus, the resonant frequency of the TE_{111}^y mode and the input impedance are significantly affected. The input impedance can be fine tuned by adjusting the DR offset d_s , the length of the extended microstrip line, and the aperture length L_a .

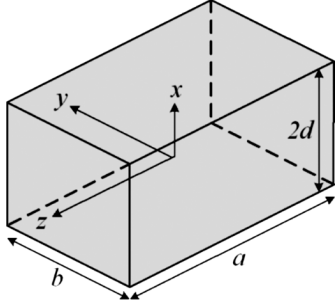


Fig. 2. Single block of dielectric resonator.

III. PREDICTION OF RESONANT FREQUENCY SHIFT

The electric field \vec{E}_0 and the magnetic field \vec{H}_0 in a dielectric resonator taking the space V satisfy the Maxwell's equations

$$-\nabla \times \vec{E}_0 = j\omega_0 \mu \vec{H}_0 \quad (1)$$

$$\nabla \times \vec{H}_0 = j\omega_0 \epsilon \vec{E}_0 \quad (2)$$

where ω_0 is the resonant frequency. When the shape of dielectric resonator is modified by engraving gap, tunnel, or notch, the dielectric constant in the space V becomes a function of location $\epsilon'(\vec{r})$ and the field distributions and the resonant frequency become \vec{E} , \vec{H} and ω , respectively, satisfying the Maxwell's equations as well. Applying the reaction operation between the original field and the perturbed field [16], the resonant frequency of the modified DR can be expressed as

$$\omega = \frac{\tilde{W}_m + \tilde{W}_{eb}}{\tilde{W}_m + \tilde{W}_{ea}} \omega_0 - \frac{j \iint_S (\vec{H} \times \vec{E}_0^* + \vec{H}_0^* \times \vec{E}) \cdot d\vec{s}}{\tilde{W}_m + \tilde{W}_{ea}} \quad (3)$$

where

$$\begin{aligned} \tilde{W}_m &= \iiint_V \mu \vec{H}_0^* \cdot \vec{H} dv \\ \tilde{W}_{ea} &= \iiint_V \epsilon(\vec{r}) \vec{E} \cdot \vec{E}_0^* dv \\ \tilde{W}_{eb} &= \iiint_V \epsilon \vec{E}_0^* \cdot \vec{E} dv \end{aligned}$$

which indicates that the resonant frequency is affected by the reaction between the field distributions of the original and the modified DR structures. It also implies that the resonant frequency can be more accurately predicted if the perturbed field can be approximated with reasonable accuracy. For example, if a small gap is carved off a DR, the electric field normal to the air-dielectric interface will be significantly enhanced, which can be observed by simulation.

IV. RECTANGULAR DIELECTRIC RESONATOR WITH SHAPE MODIFICATIONS

A DR of dimension $d \times b \times a$ on an infinite ground plane can be viewed as a single block of rectangular dielectric with height $2d$ in free space, as shown in Fig. 2. Since the permittivity of DR is much higher than that of the air, the air-dielectric interface can

be approximated as a perfect magnetic conductor (PMC) wall in a first-order analysis [17], and the modes can be categorized into transverse electric (TE) and transverse magnetic (TM) modes [18]. It is shown that the PMC approximation gives more accurate results with the TM modes than with the TE modes [17]. The dielectric waveguide model (DWM) is proposed to render more accurate prediction, in which the DR is treated as a portion of a dielectric waveguide truncated in the propagation direction [19]–[21]. The PMC approximation is imposed on the guide surfaces and total reflection is assumed in the propagation direction. By this way, the fields of the TE_{11m}^y modes with odd m can be derived as

$$\begin{aligned} E_{0x} &= -k_z A \cos(k_x x) \cos(k_y y) \sin(k_z z) \\ E_{0y} &= 0 \\ E_{0z} &= k_x A \sin(k_x x) \cos(k_y y) \cos(k_z z) \\ H_{0x} &= \frac{k_x k_y}{j\omega\mu} A \sin(k_x x) \sin(k_y y) \cos(k_z z) \\ H_{0y} &= \frac{k_x^2 + k_z^2}{j\omega\mu} A \cos(k_x x) \cos(k_y y) \cos(k_z z) \\ H_{0z} &= \frac{k_z k_y}{j\omega\mu} A \cos(k_x x) \sin(k_y y) \sin(k_z z) \end{aligned} \quad (4)$$

where A is an arbitrary constant, $k_x = \pi/2d$, $k_z = m\pi/a$, and k_y is determined from [22]

$$\frac{k_y b}{2} = \tan^{-1} \left(\frac{\sqrt{k_x^2 + k_z^2}}{k_y} \right). \quad (5)$$

The resonant frequency can thus be calculated as

$$f_r = \frac{c}{\sqrt{\epsilon_r}} \sqrt{k_x^2 + k_y^2 + k_z^2}. \quad (6)$$

The field expressions of the TE_{11n}^y modes with even n can be derived as

$$\begin{aligned} E_{0x} &= -k_z B \cos(k_x x) \cos(k_y y) \cos(k_z z) \\ E_{0y} &= 0 \\ E_{0z} &= k_x B \sin(k_x x) \cos(k_y y) \sin(k_z z) \\ H_{0x} &= \frac{k_x k_y}{j\omega\mu} B \sin(k_x x) \sin(k_y y) \sin(k_z z) \\ H_{0y} &= \frac{k_x^2 + k_z^2}{j\omega\mu} B \cos(k_x x) \cos(k_y y) \sin(k_z z) \\ H_{0z} &= -\frac{k_z k_y}{j\omega\mu} B \cos(k_x x) \sin(k_y y) \cos(k_z z) \end{aligned} \quad (7)$$

where B is an arbitrary constant, $k_x = \pi/2d$, $k_z = n\pi/a$, k_y and the resonant frequency can be determined from (5) and (6), respectively.

Fig. 3 illustrates the electric field distributions of the first three modes indexed by the third suffix, which indicates the number of variations of the electric field in the DR. The E_z component along the z -axis has an odd number of variations for the odd modes and has an even number of variations for the even modes. The E_x component is antisymmetric with respect to the x -axis for the odd modes and is symmetric for the even modes.

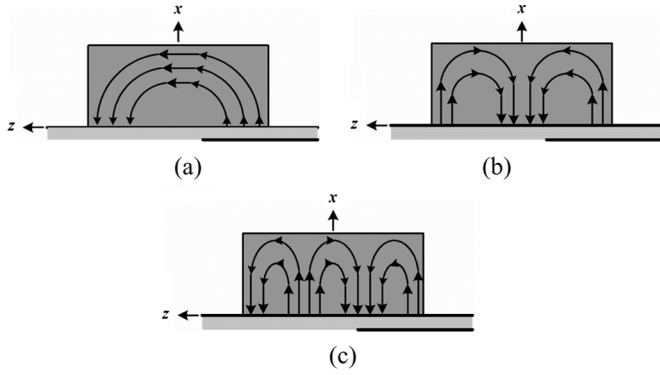


Fig. 3. Electric field distribution of (a) TE_{111}^y mode, (b) TE_{112}^y mode, and (c) TE_{113}^y mode of a solid DR.

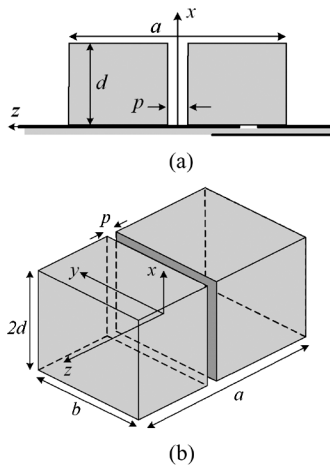


Fig. 4. (a) DRs on a ground plane with gap in between. (b) Panoramic view of the equivalent problem.

A. Field Enhancement by a Gap

Fig. 4(a) shows two rectangular DRs placed on a ground plane, separated by a gap at $z = 0$. At $z = 0$, E_z component of the TE_{111}^y and TE_{113}^y modes reaches the maximum while that of the TE_{112}^y mode vanishes. The gap p is much smaller than a and the resonant modes associated with the single DR formed by filling the gap between the aforementioned two DRs are excited. The air-dielectric interface of the gap is normal to \hat{z} , hence the E_z component is significantly enhanced to satisfy the continuity condition on D_z .

Fig. 5 shows the effect of gap width p on the return loss. It is observed that the resonant frequency of the TE_{111}^y mode increases significantly, while those of the TE_{112}^y and TE_{113}^y modes are slightly affected. Note that the band associated with the TE_{111}^y mode merges with that of the TE_{112}^y mode.

By image theory, the structure in Fig. 4(a) is equivalent to that in Fig. 4(b) if the ground plane is of infinite extent. The two DRs with a separating gap can be regarded as an inhomogeneous DR with permittivity $\epsilon'(\vec{r})$. The gap width p is assumed much smaller than a , hence the field distribution inside the single inhomogeneous DR is almost the same as that without the gap, except the normal electric field E_z inside the gap is enhanced to satisfy the air-dielectric continuity condition. Thus, the fields of

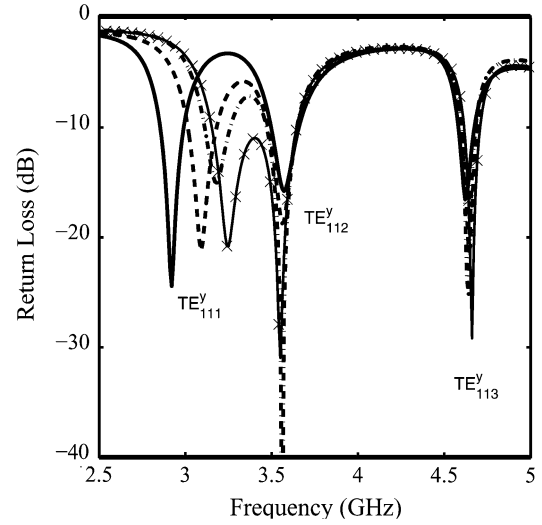


Fig. 5. Effect of gap width p on return loss, $a = 28$ mm, $b = 9$ mm, $d = 10$ mm, $\epsilon_r = 20$, $w_a = 2$ mm, $L_a = 10$ mm, $L_s = 8$ mm, $d_s = 7$ mm, $W_g = L_g = 70$ mm, $t = 0.6$ mm, $w_m = 1.15$ mm. (—) $p = 0$ mm. (---) $p = 0.2$ mm. (- · -) $p = 0.4$ mm. (- × -) $p = 0.5$ mm.

TABLE I
COMPARISON OF RESONANT FREQUENCY SHIFT DUE TO GAP WIDTH;
FREQUENCY UNIT: GIGAHERTZ, LENGTH UNIT: MILLIMETER

| $f_r(\Delta f)$ | $p = 0.1$ | $p = 0.2$ | $p = 0.4$ | $p = 0.5$ |
|-----------------|---------------|---------------|---------------|--------------|
| HFSS | 3.03 (0.1) | 3.11 (0.18) | 3.25 (0.33) | 3.3 (0.37) |
| Theory | 2.93 (0.1) | 3.03 (0.2) | 3.23 (0.41) | 3.33 (0.51) |
| (TE_{111}^y) | | | | |
| HFSS | 3.65 (0.01) | 3.67 (0.03) | 3.65 (0.01) | 3.66 (0.02) |
| Theory | 3.666 (0.014) | 3.673 (0.028) | 3.669 (0.056) | 3.696 (0.07) |
| (TE_{112}^y) | | | | |
| HFSS | 4.64 (0.01) | 4.65 (0.02) | 4.66 (0.03) | 4.67 (0.04) |
| Theory | 4.7 (0.02) | 4.755 (0.04) | 4.86 (0.05) | 4.92 (0.07) |
| (TE_{113}^y) | | | | |

the TE_{111}^y and TE_{113}^y modes in the air gap can be approximated as

$$\begin{aligned} E_z &= m_1 k_x A \sin(k_x x) \cos(k_y y) \cos(k_z p/2) \\ E_x &= E_y \simeq 0 \\ \vec{H} &= \vec{H}_0. \end{aligned} \quad (8)$$

Note that the E_z component is enhanced by a factor m_1 . For the TE_{111}^y mode, m_1 approaches ϵ_r as the gap width is very small. For the TE_{113}^y mode, it is observed that the E_z component is only slightly enhanced, incurring a small m_1 of about 2 to 3. Hence, the resonant frequency of the TE_{113}^y mode is slightly increased. In contrast, the fields of the TE_{112}^y modes in the air gap are approximately

$$\begin{aligned} E_x &= k_z B \cos(k_y y) \cos(k_x x) \\ E_z &= E_y \simeq 0 \\ \vec{H} &= \vec{H}_0. \end{aligned} \quad (9)$$

Substituting (4) and (8) with $k_z = \pi/a$ and $k_z = 3\pi/a$, respectively, into (3), the resonant frequencies of the TE_{111}^y and TE_{113}^y modes can be estimated. Substituting (7) and (9) with $k_z = 2\pi/a$ into (3), the resonant frequency of the TE_{112}^y mode can be estimated. The theoretical prediction and simulated results are summarized in Table I. The resonant frequency of the DR is also affected by the feeding position, resulting in a deviation between

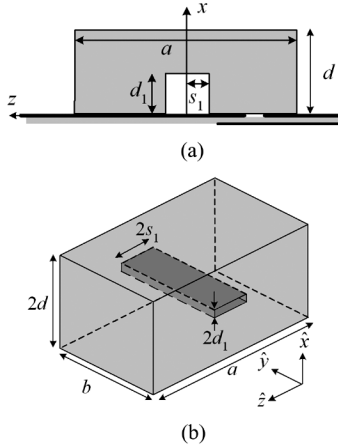


Fig. 6. (a) DR on ground plane with tunnel engraved at its bottom. (b) Equivalent problem of DR in free space with a tunnel.

simulation and prediction. Note that the increments of resonant frequency listed in the parentheses match reasonably well.

The radiation patterns can be determined from the tangential electric fields on the DR surfaces. Since the electric field distribution of the TE_{112}^y mode $E_z \propto \sin(2\pi z/a)$ has opposite directions on different portions of the DR top surface, a null in the E_θ pattern occurs in the \hat{x} -direction. The resonant frequencies of the TE_{111}^y and TE_{112}^y modes move closer as p is increased and the two bands are merged at $p = 0.5$ mm. However, due to the difference of radiation pattern, it is preferred to separate the band associated with the TE_{112}^y mode from that with the TE_{111}^y mode.

B. Effect of an Air Tunnel

Based on (3), the resonant frequency of the TE_{112}^y mode can be shifted away from that of the TE_{111}^y mode if an air tunnel is engraved at where the electric field of the TE_{112}^y mode is strong while that of the TE_{111}^y mode is negligible. As shown in Fig. 6(a), an air tunnel is engraved at the center bottom of the DR with the dimensions of $d_1 \times b \times 2s_1$. The effect of the tunnel half-width s_1 is shown in Fig. 7. The resonant frequency of the TE_{112}^y mode is increased as s_1 and d_1 increase, while those of the TE_{111}^y and TE_{113}^y modes are almost unaffected since their electric field at the tunnel is weak.

Fig. 6(b) shows an equivalent problem in free space by doubling the heights of the DR and the tunnel using the image theory. Since the electric field of the TE_{111}^y and the TE_{113}^y modes rotates about the \hat{y} -axis, the field is tangential to the air-dielectric interface of the tunnel. Hence, it is reasonable to assume that $\vec{E} \simeq \vec{E}_0$ and $\vec{H} \simeq \vec{H}_0$.

As for the TE_{112}^y mode, the tunnel is located at where the electric field reaches the maximum. The E_x component is enhanced in the tunnel and can be approximated as

$$\begin{aligned} E_x &= k_z \alpha B \cos(k_x d_1) \cos(k_y y) \cos(\beta z) \\ E_z &= E_y \simeq 0 \\ \vec{H} &= \vec{H}_0. \end{aligned} \quad (10)$$

By observing the simulated field distributions and fitting the data, we record $\alpha \simeq 10$ and $\beta \simeq 568.8$ at $d_1 = 0.5$ mm, $\alpha \simeq 1.5$ and $\beta \simeq 275$ at $d_1 = 4$ mm. Substituting (7) and

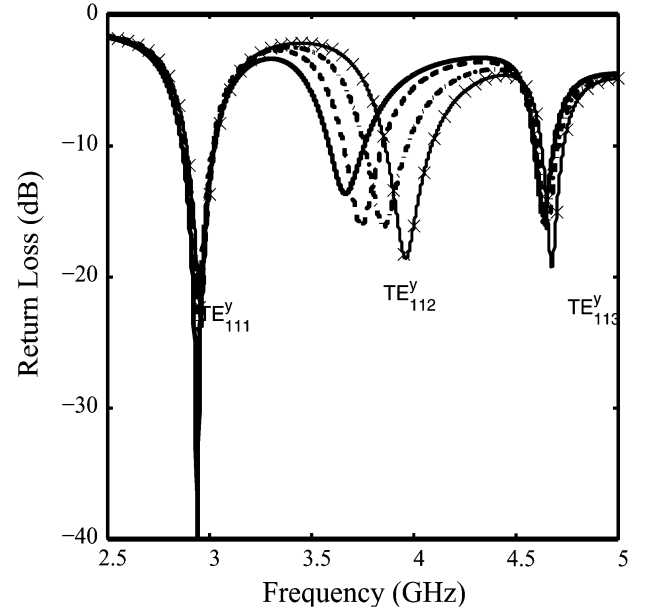


Fig. 7. Effect of s_1 on return loss, $a = 28$ mm, $b = 9$ mm, $d = 10$ mm, $p = 0$ mm, $d_1 = 4$ mm, $\epsilon_r = 20$, $w_a = 2$ mm, $L_a = 10$ mm, $L_s = 8$ mm, $d_s = 7$ mm, $W_g = L_g = 70$ mm, $t = 0.6$ mm, $w_m = 1.15$ mm. (—) $s_1 = 0.5$ mm. (---) $s_1 = 1$ mm. (- · -) $s_1 = 1.5$ mm. (- - -) $s_1 = 2$ mm.

TABLE II
COMPARISON OF RESONANT FREQUENCY SHIFT DUE TO TUNNEL WIDTH;
LENGTH UNIT: MILLIMETER, FREQUENCY UNIT: GIGAHERTZ

| $f_r(\Delta f)$ | $s_1 = 0.5$ | $s_1 = 1$ | $s_1 = 1.5$ | $s_1 = 2$ |
|-----------------|--------------|---------------|--------------|--------------|
| TE_{111}^y | | | | |
| HFSS | 2.93 (0.01) | 2.94 (0.02) | 2.94 (0.02) | 2.95 (0.03) |
| Theory | 2.83 (0.008) | 2.844 (0.015) | 2.85 (0.023) | 2.86 (0.032) |
| $d_1 = 4$ | | | | |
| TE_{112}^y | | | | |
| HFSS | 3.6 (0.02) | 3.64 (0.06) | 3.67 (0.09) | 3.73 (0.15) |
| Theory | 3.68 (0.03) | 3.7 (0.05) | 3.72 (0.07) | 3.73 (0.08) |
| $d_1 = 0.5$ | | | | |
| $\alpha = 10$ | | | | |
| TE_{112}^y | | | | |
| HFSS | 3.67 (0.07) | 3.74 (0.14) | 3.85 (0.25) | 3.96 (0.33) |
| Theory | 3.74 (0.08) | 3.82 (0.165) | 3.91 (0.246) | 3.98 (0.323) |
| $d_1 = 4$ | | | | |
| $\alpha = 1.5$ | | | | |
| TE_{113}^y | | | | |
| HFSS | 4.63 (0.01) | 4.63 (0.01) | 4.65 (0.03) | 4.67 (0.05) |
| Theory | 4.65 (0.004) | 4.66 (0.013) | 4.68 (0.032) | 4.71 (0.066) |
| $d_1 = 4$ | | | | |

(10) with $k_z = 2\pi/a$ into (3), the resonant frequency shift of the TE_{112}^y mode is predicted. The simulated and predicted results are summarized in Table II. The tunnel has stronger effect on the resonant frequency of the TE_{112}^y mode than that of the TE_{111}^y and TE_{113}^y modes. Hence, the effect of tunnel height of $d_1 = 0.5$ mm and $d_1 = 4$ mm, respectively, is investigated and listed in Table II. It is observed that the E_x is strongly enhanced by α fold as the tunnel is thin. The resonant frequency f_r of the TE_{112}^y mode is 3.646 GHz. The increments of resonant frequency listed in the parentheses match reasonably well.

C. Modification by Engraving Notches

Since the E_x component of the TE_{111}^y , TE_{112}^y , and TE_{113}^y modes reaches maximum at $z = \pm a/2$, their resonant frequencies should be affected by notches near $z = \pm a/2$. Fig. 8(a)

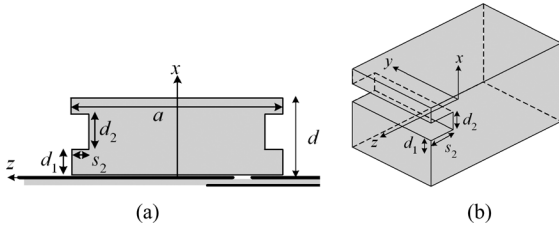


Fig. 8. (a) Grounded dielectric resonator with two notches on its edges. (b) Panoramic view of an isolated DR with one notch.

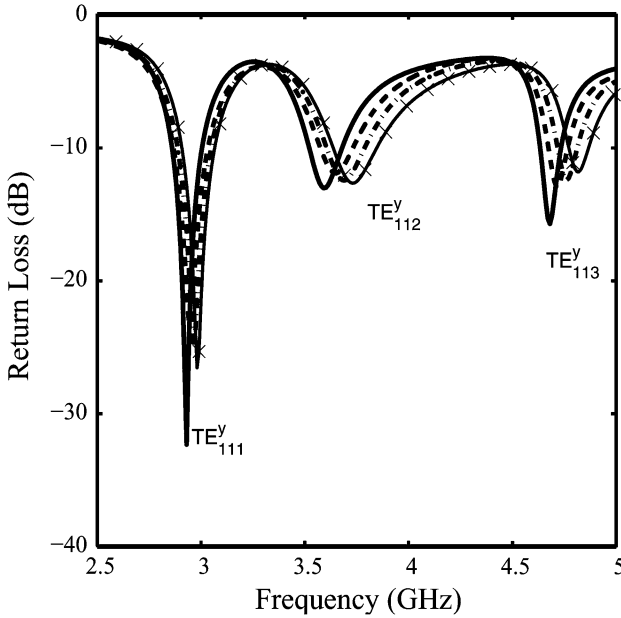


Fig. 9. Effect of s_2 on return loss, $a = 28$ mm, $b = 9$ mm, $d = 10$ mm, $\epsilon_r = 20$, $w_a = 2$ mm, $L_a = 10$ mm, $L_s = 8$ mm, $d_s = 7$ mm, $W_g = L_g = 70$ mm, $t = 0.6$ mm, $w_m = 1.15$ mm. (—) $s_2 = 0.5$ mm. (---) $s_2 = 1$ mm. (- · -) $s_2 = 1.5$ mm. (- × -) $s_2 = 2$ mm.

TABLE III

COMPARISON OF RESONANT FREQUENCY SHIFT DUE TO NOTCH DEPTH $m_2 = 1.5$; LENGTH UNIT: MILLIMETER, FREQUENCY UNIT: GIGAHERTZ

| $f_r(\Delta f)$ (GHz) | $s_2 = 0.5$ | $s_2 = 1$ | $s_2 = 1.5$ | $s_2 = 2$ |
|-----------------------|-------------|-------------|-------------|-------------|
| HFSS | 2.93 (0.01) | 2.95 (0.04) | 2.96 (0.05) | 2.98 (0.07) |
| Theory | 2.86 (0.03) | 2.89 (0.06) | 2.92 (0.09) | 2.95 (0.12) |
| TE_{111}^y | | | | |
| HFSS | 3.59 (0.01) | 3.65 (0.07) | 3.69 (0.11) | 3.73 (0.15) |
| Theory | 3.71 (0.06) | 3.78 (0.12) | 3.84 (0.18) | 3.9 (0.23) |
| TE_{112}^y | | | | |
| HFSS | 4.68 (0.04) | 4.72 (0.08) | 4.76 (0.12) | 4.82 (0.18) |
| Theory | 4.75(0.11) | 4.85(0.21) | 4.94(0.30) | 5.02(0.37) |
| TE_{113}^y | | | | |

shows a grounded DRA with two notches engraved around its edge. The notches will distort the electric field distribution and the Q -factor of the DR will decrease, incurring a wider impedance bandwidth. Fig. 9 shows that the resonant frequencies of the three modes are increased by increasing the notch depth s_2 .

By image theory, the grounded DR with two notches is equivalent to an isolated DR with four notches on its edges. First, consider only one notch of dimensions $d_2 \times b \times s_2$ engraved off a DR in free space, as shown in Fig. 8(b). The electric field within the notch is more complicated since both E_x and E_z components exist. The simulation show that the E_x component is stronger

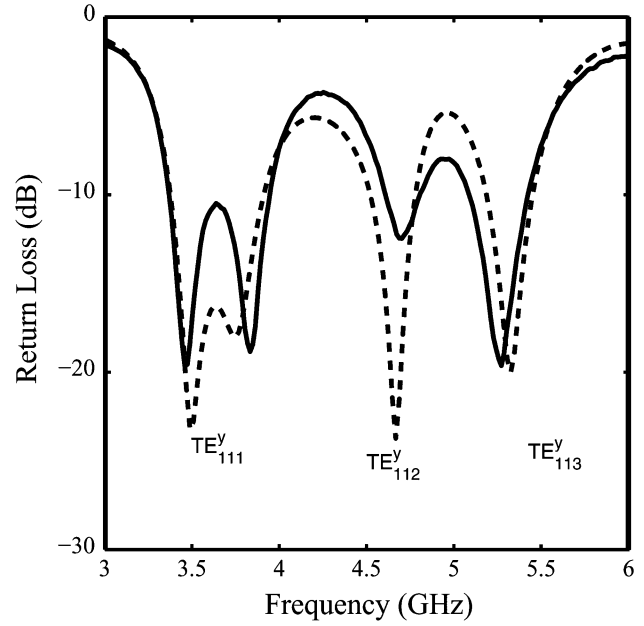


Fig. 10. Return loss, $a = 28$ mm, $b = 9$ mm, $d = 10$ mm, $p = 1$ mm, $d_1 = 4$ mm, $s_1 = 2$ mm, $d_2 = 4$ mm, $s_2 = 2$ mm, $\epsilon_r = 20$, $h = 4$ mm, $w_a = 2$ mm, $L_a = 10$ mm, $L_s = 2.5$ mm, $d_s = 4$ mm, $W_g = L_g = 70$ mm, $t = 0.6$ mm, $w_m = 1.15$ mm. (—) Measurement. (---) Simulation.

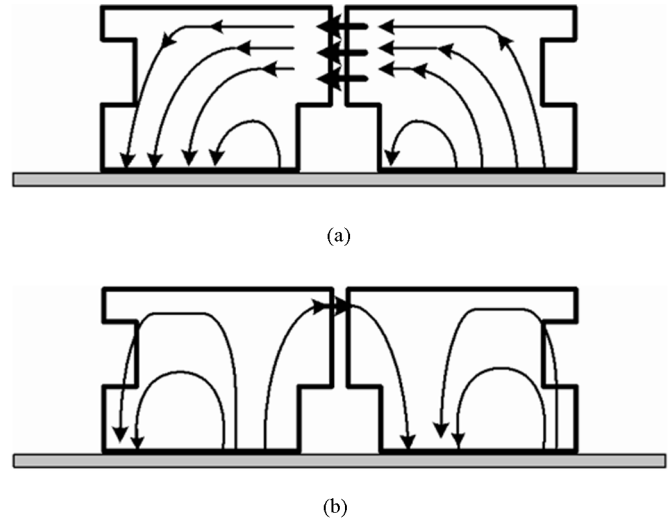


Fig. 11. Electric field distribution at (a) 3.45 and (b) 5.26 GHz.

than the E_z component. The E_x component normal to the air-dielectric interface of the notch is enhanced to satisfy the continuity condition and can be approximated as

$$E_x = -m_2 k_z A \cos(k_x d_1) \cos(k_y y) \sin(k_z z),$$

for TE_{111}^y and TE_{113}^y modes (11)

$$E_x = m_2 k_z B \cos(k_x d_1) \cos(k_y y) \cos(k_z z),$$

for TE_{112}^y modes. (12)

With $d_2 = 4$ mm, m_2 is about 1.5. Substituting (4) and (11) into (3), the resonant frequencies of the DR with notches are obtained. The predicted and the simulated results are summarized in Table III. The prediction for the TE_{113}^y mode is less accurate, but the increasing trend is consistent.

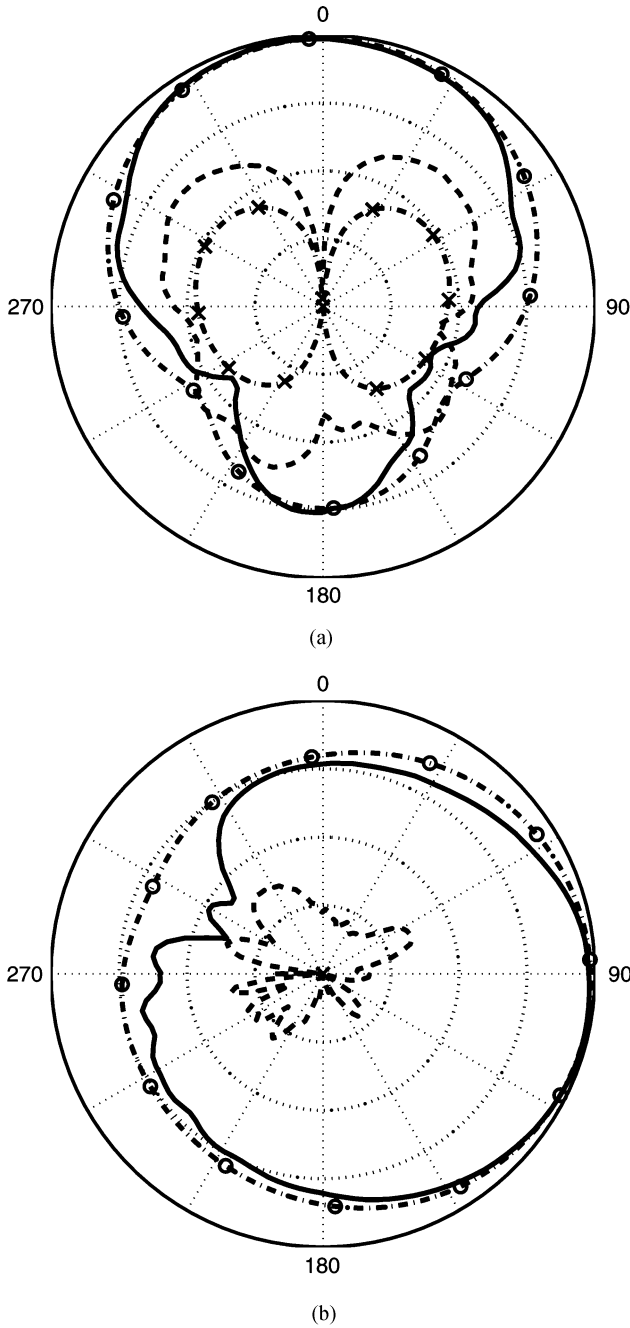


Fig. 12. Radiation patterns at $f = 3.45$ GHz: (a) xy -plane and (b) xz -plane. (—) Measured E_θ . (---) Measured E_ϕ . (-o-) Simulated E_θ . (-x-) Simulated E_ϕ , the gain at $\theta = 90^\circ$ and $\phi = 0^\circ$ is 5.6 dBi, 10-dB per division on radials; all parameters are the same as in Fig. 10.

V. DESIGN WITH COMBINATION

The design begins with a rectangular DR of dimension $10 \text{ mm} \times 9 \text{ mm} \times 29 \text{ mm}$, $d_s = 7 \text{ mm}$, $L_s = 8 \text{ mm}$, $w_a = 2 \text{ mm}$, and $L_a = 10 \text{ mm}$. The resonant frequencies of the TE_{111}^y , TE_{112}^y , and TE_{113}^y modes are 2.92, 3.58, and 4.62 GHz, respectively. In order to tune the resonant frequencies of the TE_{111}^y and TE_{113}^y modes to cover the WiMax (3.4–3.7-GHz) and the WLAN (5.15–5.35-GHz) bands, the DR is modified to the shape as shown in Fig. 1(a), with $p = 1 \text{ mm}$, $d_1 = d_2 = 4 \text{ mm}$, and $s_1 = s_2 = 2 \text{ mm}$. The resonant frequencies of the three modes are shifted to 3.58, 4.3, and 5 GHz, respectively. By adjusting

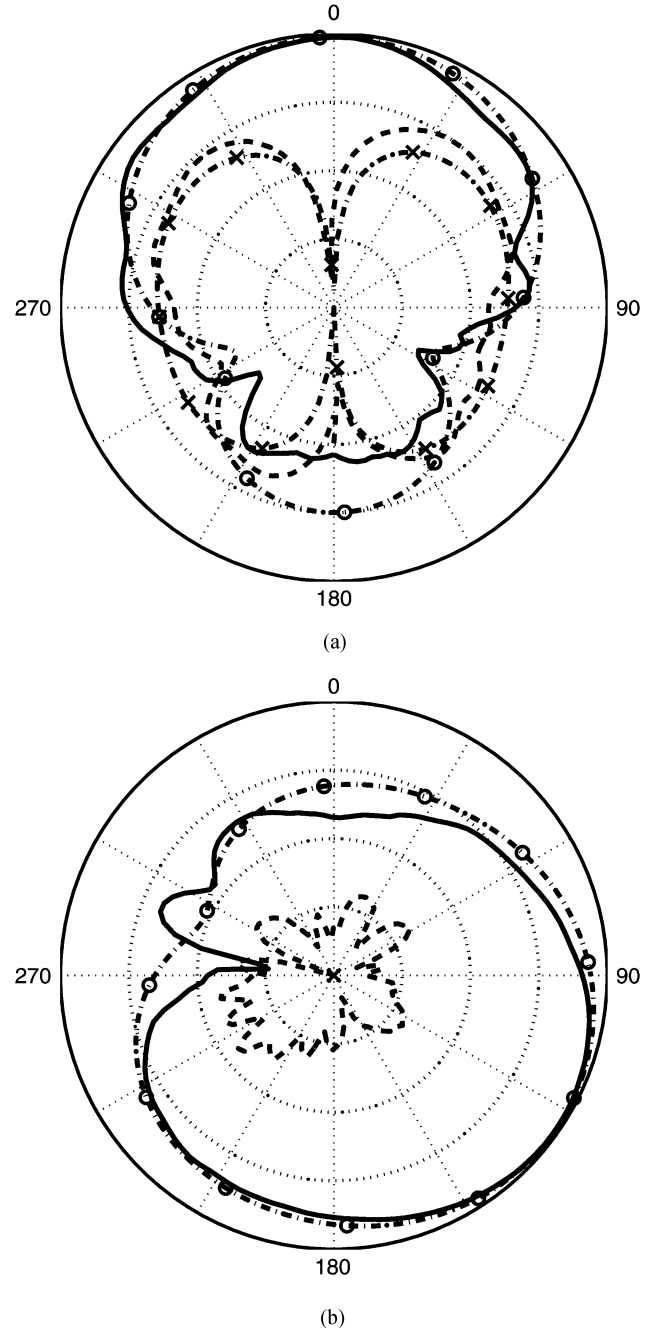


Fig. 13. Radiation patterns at $f = 3.6$ GHz: (a) xy -plane and (b) xz -plane. (—) Measured E_θ . (---) Measured E_ϕ . (-o-) Simulated E_θ . (-x-) Simulated E_ϕ , the gain at $\theta = 90^\circ$ and $\phi = 0^\circ$ is 3 dBi, 10-dB per division on radials; all parameters are the same as in Fig. 10.

the offset d_s , the extended length of microstrip line L_s , and the length of the aperture L_a , the DR can be matched to 50Ω microstrip line feed, with the resonant frequencies slightly affected by the feeding structure. Fig. 10 shows the measured and simulated return loss. There are three bands over 3.375–3.93 GHz (15%), 4.6–4.79 GHz (4%), and 5.08–5.415 GHz (6%), associated with the TE_{111}^y , TE_{112}^y , and TE_{113}^y modes, respectively. The first band covers the WiMax (3.4–3.7 GHz) and the third band covers the WLAN (5.15–5.35 GHz).

Fig. 11 shows the electric field distributions over the first and the third bands, respectively. The third resonant band around

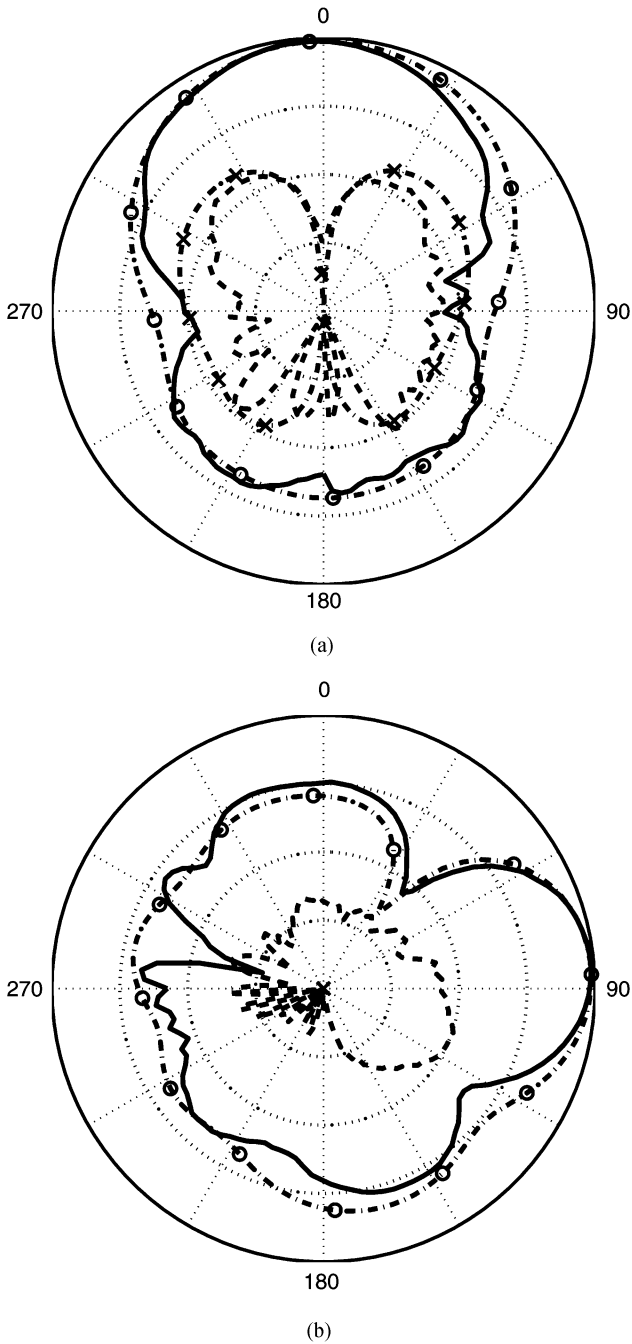


Fig. 14. Radiation pattern at 5.265 GHz: (a) xy -plane and (b) xz -plane. (—) Measured E_θ . (---) Measured E_ϕ . (—○—) Simulated E_θ . (—×—) Simulated E_ϕ , the gain at $\theta = 90^\circ$ and $\phi = 0^\circ$ is 7.2 dBi, 10-dB per division on radials; all parameters are the same as in Fig. 10.

$f = 5.265$ GHz is associated with the TE_{113}^y mode. The split DRs can be viewed as two radiators placed closely along the \hat{z} -direction.

Figs. 12 and 13 show the measured and simulated radiation patterns at $f = 3.45$ GHz and $f = 3.6$ GHz, respectively. On the xy -plane, the E_θ component is stronger than the E_ϕ component by about 10 dB over $-60^\circ \leq \phi \leq 60^\circ$, the maximum gain is 5.6 dBi at $f = 3.45$ and 3 dBi at $f = 3.6$ GHz. The gain at 3.6 GHz is lower because the main beam of the E_θ pattern is slightly tilted on the xz -plane.

On the xz -plane, the E_θ component is stronger than the E_ϕ component by 10 dB over $-90^\circ \leq \theta \leq 90^\circ$ and the maximum gain is 6.5 dBi at $f = 3.45$ GHz and 6 dBi at $f = 3.6$ GHz. The front-to-back ratio is about 10 dB.

Fig. 14 shows the measured and simulated radiation patterns at $f = 5.265$ GHz. On the xy -plane, the E_θ component is stronger than the E_ϕ component by about 10 dB over $-75^\circ \leq \phi \leq 75^\circ$, and the front-to-back ratio is about 12 dB. The antenna gain is 7.22 dBi, which is higher than that at $f = 3.45$ and 3.6 GHz because the beam of the E_θ pattern on the xz -plane is narrower and is slightly tilted to $\theta = 85^\circ$. The gain at the beam direction is 8.4 dBi.

The efficiency is about 94% for the TE_{111}^y and TE_{113}^y modes. The insertion loss of the feeding microstrip is about 0.5 dB due to the substrate loss. For WiMax or WLAN applications, this DRA can be mounted on a vertical wall with the \hat{z} -axis pointing to zenith, providing a broadside, vertically polarized radiation pattern in front of the wall (\hat{x} -direction).

VI. CONCLUSION

A dualband DRA is proposed, which is composed of two notched DRs separated by a narrow air gap. The effects of gap and notches on the resonant frequency shift are carefully studied. Two bands are attained in 3.375–3.93 GHz (15%) and 5.08–5.415 GHz (6%) with broadside E_θ pattern on the xy -plane; the third band in 4.6–4.79 GHz (4%) is not practical. The proposed DRA can be used in the WiMAX (3.4–3.7 GHz) and WLAN (5.15–5.35 GHz) bands.

REFERENCES

- [1] S. A. Long, M. W. McAllister, and L. C. Shen, "The resonant cylindrical dielectric cavity antenna," *IEEE Trans. Antennas Propag.*, vol. AP-31, no. 3, pp. 406–412, May 1983.
- [2] T. A. Denidni, Q. Rao, and A. R. Sebak, "Multi-eccentric ring slot-fed dielectric resonator antennas for multi-frequency operations," in *IEEE Int. Symp. Antennas Propag.*, Jun. 2004, vol. 2, pp. 1379–1382.
- [3] T. A. Denidni and Q. Rao, "Hybrid dielectric resonator antennas with radiating slot for dual-frequency operation," *IEEE Antennas Wireless Propag. Lett.*, vol. 3, no. 1, pp. 321–323, Dec. 2004.
- [4] A. Buerkle, K. Sarabandi, and H. Mosallaei, "Compact slot and dielectric resonator antenna with dual-resonance, broadband characteristics," *IEEE Trans. Antennas Propag.*, vol. 53, no. 3, pp. 1020–1027, Mar. 2005.
- [5] T. W. Li and J. S. Sun, "Dual-frequency dielectric resonator antenna with inverse T-shape parasitic strip," in *IEEE Appl. Comput. Electromagn. Soc. Int. Conf.*, Apr. 2005, pp. 384–387.
- [6] L. T. Wei and S. J. Shiun, "Wideband dielectric resonator antenna with parasitic strip," in *IEEE Appl. Comput. Electromagn. Soc. Int. Conf.*, Apr. 2005, pp. 376–379.
- [7] B. Li and K. W. Leung, "Strip-fed rectangular dielectric resonator antennas with/without a parasitic patch," *IEEE Trans. Antennas Propag.*, vol. 53, no. 7, pp. 2200–2207, Jul. 2005.
- [8] C. S. D. Young and S. A. Long, "Investigation of dual mode wide-band rectangular and cylindrical dielectric resonator antennas," in *Proc. IEEE Int. Symp. Antennas Propag.*, Jul. 2005, vol. 4, pp. 210–213.
- [9] A. A. Kishk, "Wide-band truncated tetrahedron dielectric resonator antenna excited by a coaxial probe," *IEEE Trans. Antennas Propag.*, vol. 51, no. 10, pp. 2913–2917, Oct. 2003.
- [10] A. A. Kishk, Y. Yin, and A. W. Glisson, "Conical dielectric resonator antennas for wide-band applications," *IEEE Trans. Antennas Propag.*, vol. 50, no. 4, pp. 469–474, Apr. 2002.
- [11] J. I. Moon and S. O. Park, "Dielectric resonator antenna for dual-band PCS/IMT-2000," *Electron. Lett.*, vol. 36, pp. 1002–1003, Jun. 2000.
- [12] Z. Fan and Y. M. M. Antar, "Experimental investigation of multi-element dielectric resonator antennas," in *IEEE Int. Symp. Antennas Propag.*, Jul. 1996, vol. 3, pp. 2034–2037.

- [13] Z. Fan and Y. M. M. Antar, "Slot-coupled DR antenna for dual-frequency operation," *IEEE Trans. Antenna Propag.*, vol. 45, no. 2, pp. 306–308, Feb. 1997.
- [14] A. A. Kishk, B. Ahn, and D. Kajfez, "Broadband stacked dielectric resonator antenna," *Electron. Lett.*, vol. 25, no. 18, pp. 1232–1233, Aug. 1989.
- [15] K. Pliakostathis and D. Mirshekar-Syahkal, "Stepped dielectric resonator antennas for wideband applications," in *IEEE Int. Symp. Antennas Propag.*, Jun. 2004, vol. 2, pp. 1367–1370.
- [16] R. F. Harrington, *Time-Harmonic Electromagnetic Fields*. New York: McGraw-Hill, 1961.
- [17] H. Y. Yee, "Natural resonant frequencies of microwave dielectric resonators," *IEEE Trans. Microw. Theory Tech.*, vol. MMT-13, no. 2, pp. 256–256, Mar. 1965.
- [18] A. K. Okaya and L. F. Barash, "The dielectric microwave resonator," *Proc. IRE*, vol. 50, no. 10, pp. 2081–2092, Oct. 1962.
- [19] T. Itoh and C. Chang, "Resonant characteristics of dielectric resonators for millimeter-wave integrated circuits," in *Proc. IEEE Microw. Theory Tech. Soc. Int. Symp.*, Jun. 1978, vol. 78, pp. 121–122.
- [20] R. K. Mongia, "Theoretical and experimental resonant frequencies of rectangular dielectric resonators," in *Proc. Inst. Electr. Eng. Microw. Antennas Propag.*, Feb. 1992, vol. 139, no. 1, pp. 98–104.
- [21] R. K. Mongia and A. Ittipiboon, "Theoretical and experimental investigations on rectangular dielectric resonator antennas," *IEEE Trans. Antennas Propag.*, vol. 45, no. 9, pp. 1348–1356, Sep. 1997.
- [22] Y. M. M. Antar, D. Cheng, G. Seguin, B. Henry, and M. G. Keller, "Modified waveguide model (MWGM) for rectangular resonator antenna (DRA)," *Microw. Opt. Tech. Lett.*, vol. 19, no. 2, pp. 158–160, Oct. 1998.



Tze-Hsuan Chang (S'01) was born in Hsin-Chu, Taiwan, on February 1, 1978. He received the B.S. degree in electrical engineering from the National Chung Hsing University, Taichung, Taiwan, in July 2000 and the Ph.D. degree in electrical engineering from in the Graduate Institute of Communication Engineering, National Taiwan University, Taipei, Taiwan, in July 2007.



Jean-Fu Kiang (M'89) was born in Taipei, Taiwan, on February 2, 1957. He received the B.S. and M.S. degrees from National Taiwan University, Taipei, Taiwan, and the Ph.D. degree from Massachusetts Institute of Technology, Cambridge, in 1979, 1981, and 1989, respectively, all in electrical engineering.

He was with Schlumberger-Doll Research, Ridgefield, CT, in 1985–1986, IBM Watson Research Center, Yorktown Heights, NY, in 1989–1990, Bellcore, Red Bank, NJ, in 1990–1992, Siemens Electromedical Systems, Danvers, MA, in 1992–1994, and National Chung-Hsing University, Taichung, Taiwan, in 1994–1999. He has been the Professor at the Department of Electrical Engineering and the Graduate Institute of Communication Engineering, National Taiwan University since 1999. His research interests are the applications and system issues on electromagnetics, including wireless communications, antennas, electromagnetic compatibility, microwave components, etc.